A Novel Source Current Control Strategy and Its Stability Analysis for an Indirect Matrix Converter

Na Han, Bo Zhou, Jiang Yu, Xianhui Qin, Jiaxing Lei, *Student Member, IEEE*, and Yang Yang

***Abstract*—Indirect matrix converter (IMC)'s source current may contain low-order harmonics caused by asymmetric modulation in a variable-speed-constant frequency generation system. However, without capacitor/inductor decoupling effect, IMC's source current depends on loads and cannot be controlled independently. In this paper, the expressions of source current harmonics in the synchronous rotating reference frame are analyzed first. It leads to the conclusions that the only uncontrollable part of the source current is its *d*-axis dc component, and the quality of the source current can be improved by suppressing the harmonics. On the basis of above analysis, a novel source current control strategy is proposed for an IMC with asymmetric modulation, which can improve the source current quality and correct the input power factor. Self-tuning resonant controllers and a proportional integral controller are employed to achieve above goals. The stability of the system is also analyzed considering the change of input impendence after adding the source current control, which can be used as the guidance for the selection of control parameters. Finally, the validity and the feasibility of the control strategy are verified via experiments.**

***Index Terms*—Asymmetric modulation, indirect matrix converter (IMC), self-tuning resonant controller (STRC), source current control, stability analysis.**

NOMENCLATURE

$\overrightarrow{e}$	Source voltage $[e_a, e_b, e_c]^T/[e_d, e_q]^T$.
$\overrightarrow{i_s}$	Source current $[i_{\rm sa}, i_{\rm sb}, i_{\rm sc}]^T/[i_{\rm sd}, i_{\rm sq}]^T$.
$\overrightarrow{u_i}$	Input voltage $[u_{\rm ia}, u_{\rm ib}, u_{\rm ic}]^T/[u_{\rm id}, u_{\rm iq}]^T$.
$\overrightarrow{i_i}$	Input current $[i_{\rm ia}, i_{\rm ib}, i_{\rm ic}]^T/[i_{\rm id}, i_{\rm iq}]^T$.
$\overrightarrow{u_f}$	Output voltage $[u_{\rm fu}, u_{\rm fv}, u_{\rm fw}]^T/[u_{\rm fd}, u_{\rm fq}]$.
$\overrightarrow{i_f}$	Output current $[i_{\rm fu}, i_{\rm fv}, i_{\rm fw}]^T/[i_{\rm fd}, i_{\rm fq}]^T$.
$\overrightarrow{u_o}$	Load voltage $[u_{\rm ou}, u_{\rm ov}, u_{\rm ow}]^T/[u_{\rm od}, u_{\rm oq}]^T$.
$\overrightarrow{i_o}$	Load current $[i_{\rm ou}, i_{\rm ov}, i_{\rm ow}]^T/[i_{\rm od}, i_{\rm oq}]^T$.
L_s	Input filter inductor.
C_s	Input filter capacitor.
R_s	Input filter resistor.
R_d	Input filter damping resistor.
L_f	Output filter inductor.
C_f	Output filter capacitor.
R_f	Output filter resistor.

Manuscript received July 10, 2016; revised November 8, 2016; accepted November 26, 2016. Date of publication December 7, 2016; date of current version May 9, 2017. This work was supported by the National Natural Science Foundation of China under Grant 51177069. Recommended for publication by Associate Editor J. Espinoza.

N. Han, B. Zhou, X. Qin, and J. Lei are with the Jiangsu Key Laboratory of New Energy Generation and Power Conversion, College of Automation Engineering, Nanjing University of Aeronautics and Astronautics, Nanjing 210016, China (e-mail: hanna@nuaa.edu.cn; zhoubo@nuaa.edu.cn; qinxianhui.nuaa@gmail.com; ljxnuaa@nuaa.edu.cn).

J. Yu and Y. Yang are with the Aviation Key Laboratory of Science and Technology on Aerospace Power System, Shaanxi Aero Electric Co., Ltd., Xingping 713107, China (e-mail: jiang115yu@163.com; masayoung@163.com).

Color versions of one or more of the figures in this paper are available online at http://ieeexplore.ieee.org.

Digital Object Identifier 10.1109/TPEL.2016.2637062

I. INTRODUCTION

AS A DIRECT ac–ac converter, a matrix converter (MC) has the advantages of small volume, light weight, bidirectional power flow, etc. [1]. It has received substantial attention over the past two decades from academic community and from industry [2]. Apart from inheriting the merits of the direct MC, the indirect matrix converter (IMC) has simpler commutation strategy and clamp circuit [3], [4]. Thus, it has wide application prospects in variable-speed constant-frequency (VSCF) generation systems, such as military, aerospace, and wind turbine stand-alone generation system, which have high requirements but extreme working conditions [5]–[7].

Due to the lack of energy storage components, the input and output of the IMC are closely coupled, leading to a lower degree of freedom than that of the back-to-back converter [8]. It means that the phase angle of source current synthetic vector can be predetermined, but its amplitude depends on the output current and cannot be controlled independently [9]. Efforts have been made in [10] and [11] to force source current waveforms to follow a sinusoidal reference through PID control and predictive control, respectively. But results show that the source waveform improvement would actually worsen the output performance.

Influenced by wide-frequency variation range in the VSCF generation system, IMC's input frequency may be high in some cases, which is a great challenge to the control performance of the IMC. Asymmetric modulation is applied to these applications due to its simple implementation, low dissipation, small narrow pulse probability, and so on. But it is intrinsically coupled with nonlinearity. The variation of input current pulse distribution will artificially inject low-order harmonics in IMC's source current as the increasing of input frequency, resulting in harmonic pollution and loss increment [12]. Rare improving methods aiming at source current distortion caused by asymmetric modulation have been published. Only a duty ratio correction algorithm based on the difference equation is proposed in [12]. It can predict the distortion of the source current in the next period and adjust the duty cycle to improve the quality of current

waveform. This method suppresses the harmonics at the source, but error still exists due to the open-loop nature.

Different from [10] and [11] considering source current as a whole, this paper divides it into *d*-axis harmonics, *q*-axis harmonics, *d*-axis dc component, and *q*-axis dc component, whose analytic formulations are derived, respectively. Due to the ac nature of harmonics in *d*-/*q*-axis, proportional resonant (PR) control is a good choice for the system to realize closed-loop control [13]. PR control and repetitive control, which are both based on the internal model principle [14], can transform to each other. According to the principle of the repetitive control compensator, the resonant controller with a phase compensator is derived in [15] and [16], which can set different phase compensation angles at different frequencies to meet the needs of the system. Apart from the phase compensator, the resonant controller used in [17] also contains the damping coefficient to reduce the influence of the frequency detection error and facilitate the digital realization. PR controllers mentioned above are generally used in applications where variations in the resonant frequency are small. In order to operate with a suitable bandwidth and phase margin over a wide-frequency range, a self-tuning resonant controller (STRC) is adopted in [18] and [19], which is capable of adapting itself to the command of time-varying frequency. Based on above analysis, a closed-loop control strategy based on the controllable parts of the source current, namely, its *d*-/*q*-axis harmonics and *q*-axis dc component, is proposed in this paper, which adopts the STRC to minimize the low-order harmonics in source current caused by asymmetric modulation and proportional integral (PI) controller to correct the input power factor. Since the proposed method does not attempt to control source current's *d*-axis dc component, which is mainly determined by the output current, it will not degrade the output performance while improving source current waveforms, as mentioned in [10] and [11].

Further investigation on the proposed source current control strategy shows that the addition of the control strategy will change the input impedance of the IMC to a certain extent due to the feedforward control in the *d*-axis. The variation of IMC's input impedance may excite the resonance of an input *LC* filter, which is necessary for the IMC to reduce the source current ripple caused by switching [20]. Thus, the impacts of the proposed control strategy on the resonance of the input filter and the system stability are also analyzed in this paper. An active damping method is adopted to mitigate the resonance effect in the input side [21].

This paper is organized as follows. In Section II, the frequency and expressions of the source current harmonics in *dq* coordinates are analyzed according to the power balance principle in MCs. In Section III, a novel source current control strategy referring to the controllable parts of the source current is proposed, which adopts STRCs to inhibit the low-order harmonics and PI to correct the input power factor (*q*-axial dc component). In Section IV, the stability of the system is analyzed considering the change of input impendence after adding the source current control. In Section V, the validity and the feasibility of the control strategy are verified via experiments.

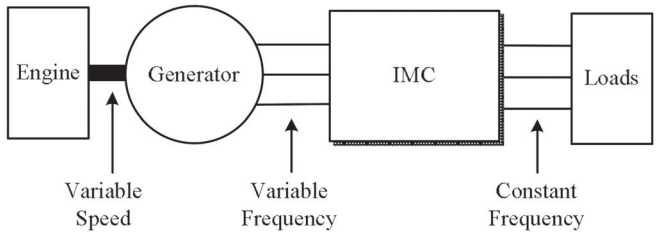

Fig. 1. Diagram of the IMC-based VSCF generation system.

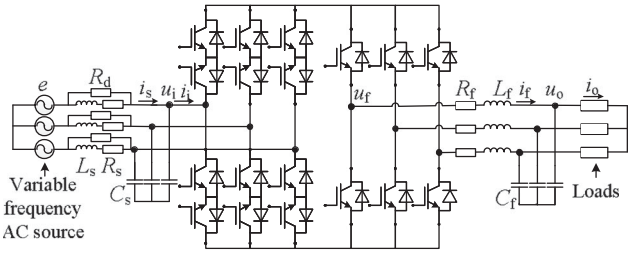

Fig. 2. Topology of the IMC in the VSCF generation system.

II. Source Current Harmonics Analysis in the Synchronous Rotating Reference Frame

The diagram of the IMC-based VSCF generation system is shown in Fig. 1. The generator is directly driven by an engine, which outputs variable-frequency voltage along with the change of engine speed. The IMC transforms the variable-frequency voltage into desired constant-frequency constant voltage ac source to satisfy the demand of loads.

The topology of the IMC in the VSCF generation system is displayed in Fig. 2. The generator is replaced by a variable-frequency ac source for simplicity. It is connected to the input side of the IMC through an *LC* filter. IMC's main power circuit is composed of a rectifier and an inverter, whose output is connected to the loads through another *LC* filter.

A. Frequency Analysis of Harmonics

Dual-space vector modulation (DSVM) is the most commonly used modulation strategy for IMC, which can be divided into two kinds: symmetric and asymmetric [22]. Their typical modulation waveforms are shown in Fig. 3, where $U_{\rm dc}$ is the dc-link instantaneous voltage and G_u, G_v, and G_w are three-phase driving signals for inverter stage.

Compared with symmetric modulation, the reduction of switch times in inverter stage is the most important feature of asymmetric modulation, which can bring the following advantages:

1) *Lower switching losses:* Although the rectifier stage of the IMC commutates at zero current, its inverter stage works in the hard switching state. The switching losses will reduce if there is a reduction in its switch times.
2) *Smaller narrow pulse probability:* When the sector angle of rectifier or inverter stage is close to 0 or $\pi/3$, the duty ratios of some space vectors are close to zero, which will be neglected if they are smaller than commutation time. This

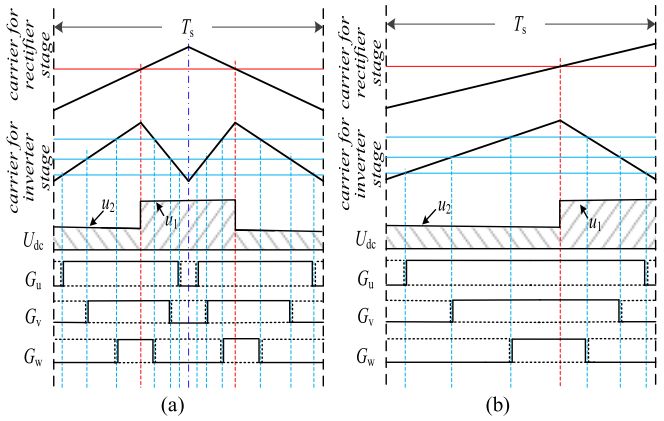

Fig. 3. DC-link voltage (U_{dc}) of the IMC and driving signals for the inverter stage (G_u, G_v, and G_w) in a single period. (a) Symmetric and (b) Asymmetric modulation.

will result in the distortion of output voltage and source current [23]. Space vectors' duty cycles of asymmetric modulation are twice of those of symmetric modulation if the two modulation methods have the same switching frequency. Thus, asymmetric modulation has smaller narrow pulse probability.

3) *Weaker dead zone effect:* The dead time, which is inserted to avoid shoot-through problems, is reduced by half in a single period. Thus, the converter suffers from a weaker dead zone effect because of the reduction of commutation times.

What is more, it is simpler in implementation and has a low-switching-frequency requirement on power devices.

Unfortunately, asymmetric modulation, which is intrinsically coupled with nonlinearity, will cause $(3n \pm 1)\omega_{in}$ $(n = 1, 2 \ldots)$ harmonics in source current, where ω_{in} is the input angular frequency of the system [12].

Assuming that the RMSs of $(3n \pm 1)\omega_{in}$ harmonics are $\Delta I_{3n\pm1}$, the current expressions in *abc* coordinates are shown as

$$\begin{bmatrix} \Delta i_{sa\_3n\pm1} \\ \Delta i_{sb\_3n\pm1} \\ \Delta i_{sc\_3n\pm1} \end{bmatrix} = \sqrt{2}\Delta I_{s\_3n\pm1} \times \begin{bmatrix} \sin[(3n \pm 1)\omega_{in}t + \varphi_{3n\pm1}] \\ \sin[(3n \pm 1)(\omega_{in}t - \frac{2}{3}\pi) + \varphi_{3n\pm1}] \\ \sin[(3n \pm 1)(\omega_{in}t + \frac{2}{3}\pi) + \varphi_{3n\pm1}] \end{bmatrix} \quad (1)$$

where $\Delta i_{sa\_3n\pm1}$, $\Delta i_{sb\_3n\pm1}$, and $\Delta i_{sc\_3n\pm1}$ are three-phase currents of $(3n \pm 1)\omega_{in}$ harmonics. $\varphi_{3n\pm1}$ is the initial phase angle of $\Delta i_{sa\_3n\pm1}$.

The expressions of current harmonics in *dq* coordinates are denoted in (2) after transforming (1) from stationary to rotating reference frame

$$\begin{bmatrix} \Delta i_{sd\_3n\pm1} \\ \Delta i_{sq\_3n\pm1} \end{bmatrix} = \sqrt{3}\Delta I_{s\_3n\pm1} \begin{bmatrix} \sin(3n\omega_{in}t + \varphi_{3n\pm1}) \\ \mp\cos(3n\omega_{in}t + \varphi_{3n\pm1}) \end{bmatrix} \quad (2)$$

where $\Delta i_{sd\_3n\pm1}$ and $\Delta i_{sq\_3n\pm1}$ are *d*- and *q*-axis components of $(3n \pm 1)\omega_{in}$ harmonics, respectively.

It can be easily concluded from (2) that IMC's source current harmonics caused by asymmetric modulation also exist in *dq* coordinates and their frequency are $3n\omega_{in}$. Qin *et al.* [12] reveals that the source current contains second-, fourth-, and fifth-order harmonics most in *abc* coordinates; thus, third- and sixth-order harmonics are the main reasons causing the source current fluctuation in *dq* coordinates.

B. Expression Analysis of Harmonics

According to the principle of power balance, the expression of input current synthetic vector can be derived as

$$\vec{i}_i = \frac{|\overrightarrow{u_f}|\left|\overrightarrow{i_f}\right|\cos\delta}{\left|\vec{u}_i\right|\cos\phi}\frac{\vec{u}_i}{\left|\vec{u}_i\right|}e^{j\phi} = \frac{u_{fd}i_{fd} + u_{fq}i_{fq}}{(u_{id}^2 + u_{iq}^2)\cos\phi}\vec{u}_i e^{j\phi} \quad (3)$$

where $|\overrightarrow{u_i}|$, $|\overrightarrow{i_i}|$, $|\overrightarrow{u_f}|$, and $|\overrightarrow{i_f}|$ represent the module values of input/output voltage/current synthetic vector; δ is the included angle between output voltage $\overrightarrow{u_f}$ and current $\overrightarrow{i_f}$; and ϕ is the included angle between input voltage $\overrightarrow{u_i}$ and current $\overrightarrow{i_i}$, which is equal to zero when the input power factor is not corrected and is a negative number if the input power factor is corrected.

d-/*q*-axis components of IMC's input current calculated from (3) are shown as

$$\begin{cases} i_{id} = \frac{u_{fd}i_{fd} + u_{fq}i_{fq}}{u_{id}^2 + u_{iq}^2}(u_{id} - u_{iq}\tan\phi) \\ i_{iq} = \frac{u_{fd}i_{fd} + u_{fq}i_{fq}}{u_{id}^2 + u_{iq}^2}(u_{iq} + u_{id}\tan\phi). \end{cases} \quad (4)$$

The input side of the IMC is directed by input voltage, which means that u_{iq} is equal to 0 all the time. According to the relationship between u_{fd}, u_{fq} and u_{od}, u_{oq} decided by the output *LC* filter, (4) can be converted to

$$\begin{cases} i_{id} = [u_{od}i_{fd} + u_{oq}i_{fq} + R_f(i_{fd}^2 + i_{fq}^2) \\ \quad\quad + \frac{1}{2}L_f\frac{d}{dt}(i_{fd}^2 + i_{fq}^2)]/u_{id} \\ i_{iq} = [u_{od}i_{fd} + u_{oq}i_{fq} + R_f(i_{fd}^2 + i_{fq}^2) \\ \quad\quad + \frac{1}{2}L_f\frac{d}{dt}(i_{fd}^2 + i_{fq}^2)]\tan\phi/u_{id}. \end{cases} \quad (5)$$

When the converter is connected with constant power loads and output control reaches steady state, i_{fd} and i_{fq} are constant dc values and the differential of $(i_{fd}^2 + i_{fq}^2)$ is small. The minor items of R_f and $\frac{d}{dt}(i_{fd}^2 + i_{fq}^2)$ can be neglected. The output side of the IMC is directed by load voltage or load current according to load characteristics, but their actual load voltage/current will track the given value, leading to u_{od}/i_{fd} being a constant value and u_{oq}/i_{fq} being zero. As a result, (5) can be simplified as

$$\begin{cases} i_{id} = u_{od}i_{fd}/u_{id} \\ i_{iq} = u_{od}i_{fd}\tan\phi/u_{id}. \end{cases} \quad (6)$$

Use *X* to denote the steady-state value of *x* and Δx to denote the harmonics of *x*. Then, the steady-state equation and the

small-signal equation around the operating point can be derived:

$$\begin{cases} I_{\rm id} = U_{\rm od} I_{\rm fd}/U_{\rm id} \\ I_{\rm iq} = U_{\rm od} I_{\rm fd} \tan\Phi/U_{\rm id} \end{cases} \tag{7}$$

$$\begin{cases} \Delta i_{\rm id} = \frac{U_{\rm od}}{U_{\rm id}} \Delta i_{\rm fd} - \frac{U_{\rm od} I_{\rm fd}}{U_{\rm id}^2} \Delta u_{\rm id} \\ \Delta i_{\rm iq} = \tan\Phi\ \Delta i_{\rm id} + \frac{U_{\rm od} I_{\rm fd}}{U_{\rm id}\cos^2\Phi} \Delta\phi. \end{cases} \tag{8}$$

The first equation of (8) shows that the harmonics of $i_{\rm id}$ are related to $\Delta i_{\rm fd}$ and $\Delta u_{\rm id}$. Harmonics contained in $i_{\rm id}$ and $u_{\rm id}$ increase and decrease simultaneously because both $i_{\rm id}$ and $u_{\rm id}$ are the state variables of the input filter. $\Delta u_{\rm id}$ can be regarded as a specific ac value, which is equal to 0 in the case of ideal source voltage. If the source voltage is distorted, $\Delta u_{\rm id}$ will be a nonzero value triggered by Δe_d, which will influence $\Delta i_{\rm id}$ undoubtedly. Unfortunately, this part of source current harmonics cannot be suppressed via internal control of the converter because it is externally motivated, which is beyond the scope of this paper and would not be discussed here. As a result, the controllable part of $\Delta i_{\rm id}$ is mainly determined by $\Delta i_{\rm fd}$, which can be marked as

$$\Delta i_{id\_\rm control} = \frac{U_{\rm od}}{U_{\rm id}} \Delta i_{\rm fd}. \tag{9}$$

According to the second equation of (8), we can know that the harmonics of $i_{\rm iq}$ are relevant to $\Delta i_{\rm id}$ and $\Delta\phi$. The value of $\Delta i_{\rm id}$ is determined by d-axis control, which should be regarded as a specific offset in the q-axis rather than the control variable. Thus, the controllable part of this equation $\Delta i_{iq\_\rm control}$ can be written as

$$\Delta i_{iq\_\rm control} = \frac{U_{\rm od} I_{\rm fd}}{U_{\rm id}\cos^2\Phi} \Delta\phi. \tag{10}$$

IMC's input current is not easy to be sampled due to its chopping nature. And it is the source current rather than the input current that connects to the power gird. As a result, source current quality is the focus of our attention, whose closed-loop control is the essence of input-side control.

For the input filter with a passive damping resistor, the transfer function from the source current $i_{\rm sd}$, $i_{\rm sq}$ to the input current $i_{\rm id}$, $i_{\rm iq}$ is given as

$$\begin{aligned} \frac{i_{sd/q}}{i_{id/q}} &= \frac{L_s s + R_d + R_s}{L_s C_s R_d s^2 + (L_s + C_s R_s R_d) s + R_d + R_s} \\ &= G_{\rm LC}(s). \end{aligned} \tag{11}$$

According to the method introduced by Qin *et al.* [24], input filter parameters are designed as follows: $L_s = 0.9$ mH, $C_s = 5\ \mu$F, $R_s = 0.1\ \Omega$, and $R_d = 40\ \Omega$. Substituting input filter parameters into (11), a certain $G_{\rm LC}(s)$ is obtained, whose bode diagram is depicted in Fig. 4 in line 1. Line 2, which will be used later, represents the phase-frequency curve having $\omega_{\rm in} T_s$ phase lag at full frequency.

Taking d-axis as an example, we can find from Fig. 4 that $G_{\rm LC}(s)$'s bode diagram can be divided into three parts. The critical frequencies are noted as ω_1 and ω_2, respectively, which can be calculated as

$$\arctan G_{\rm LC}(j\omega_1) = \varepsilon \tag{12}$$

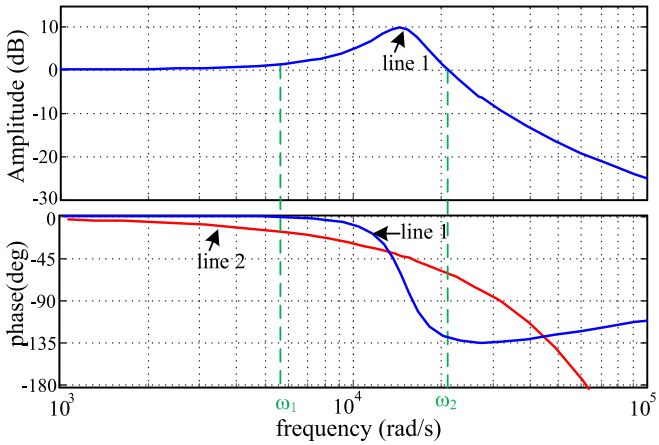

Fig. 4. Bode diagram of the input filter with a passive damping resistor.

$$\begin{cases} 20\lg|G_{\rm LC}(j\omega_2)| = 0 \\ \arctan G_{\rm LC}(j\omega_2) < 0 \end{cases} \tag{13}$$

where ε in (12) is the tolerable deviation angle decided by control requirements, which is equal to 2° in this paper.

Assuming that the harmonic of IMC's input current d-axis $\Delta i_{\rm id}$ with a frequency of $3n\omega_{\rm in}$ is expressed as $\Delta I \sin(3n\omega_{\rm in} t)$, $\Delta i_{\rm sd}$ is equal to $k\Delta I \sin(3n\omega_{\rm in} t - \varphi)$, where ΔI represents the amplitude of the harmonic, and k and φ are the amplitude ratio and phase lag angle caused by input filter resonant, respectively, whose specific values will vary with harmonics frequency. If $3n\omega_{\rm in} < \omega_1$, $k > 1$, $\varphi \asymp 0$; if $\omega_1 < 3n\omega_{\rm in} < \omega_2$, $k > 1$, $\varphi > 0$; and if $3n\omega_{\rm in} > \omega_2$, $k < 1$, $\varphi > 0$.

According to the relationship between $\Delta i_{\rm sd}$ and $\Delta i_{\rm id}$ analyzed above, (9) can be written as

$$\Delta \dot{I}_{sd\_\rm control} = \frac{kU_{\rm od}}{U_{\rm id}} \Delta \dot{I}_{\rm fd} \angle(-\varphi) \tag{14}$$

where $\Delta \dot{I}_{sd\_\rm control}$ and $\Delta \dot{I}_{\rm fd}$ represent the phasors of $\Delta i_{sd\_\rm control}$ and $\Delta i_{\rm fd}$, which can simplify the expression of the phase angle difference between two sinusoidal variables. It can be seen from (14) that there is a certain relationship between harmonics of the source current and those of the output current. $\Delta i_{\rm sd}$ can be suppressed by reducing $\Delta i_{\rm fd}$.

The conclusions above are also applicable to the q-axis, and (10) can be rewritten as follows:

$$\Delta \dot{I}_{sq\_\rm control} = \frac{kU_{\rm od} I_{\rm fd}}{U_{\rm id}\cos^2\Phi} \Delta\dot{\Phi} \angle(-\varphi) \tag{15}$$

where $\Delta \dot{I}_{sq\_\rm control}$ and $\Delta\dot{\Phi}$ represent the phasors of $\Delta i_{sq\_\rm control}$ and $\Delta\phi$. Equation (15) reveals that $\Delta i_{\rm sq}$ can be suppressed by reducing $\Delta\phi$.

Because the frequencies of source current's d-/q-axis dc components are equal to zero, $I_{sd\_\rm control}$ is equal to $I_{\rm id}$ and $I_{sq\_\rm control}$ is equal to $I_{\rm iq}$ all the time. After adding the constant values generated by the input filter capacitor, the steady-state values of d-/q-axis components of the source current can be derived

from (7):

$$\begin{cases} I_{\rm sd} = U_{\rm od} I_{\rm fd}/U_{\rm id} + I_{sd0} \\ I_{\rm sq} = U_{\rm od} I_{\rm fd} \tan\Phi/U_{\rm id} + I_{sq0} \end{cases} \quad (16)$$

where I_{sd0} and I_{sq0} are the constant currents generated by the source voltage in the input filter, which are equal to $-\omega_{\rm in} C_s u_{\rm iq}$ and $\omega_{\rm in} C_s u_{\rm id}$, respectively.

It can be learnt from (16) that the steady-state value of the source current d-axis component $I_{\rm sd}$ depends on the output current $I_{\rm fd}$ in the case of the input and load voltages being constant, which means that $I_{\rm sd}$ cannot be controlled directly. However, in addition to $I_{\rm fd}$, the steady-state value of IMC's source current q-axis component $I_{\rm sq}$ also has a relationship with included angle Φ, which means that $I_{\rm sq}$ can be controlled through Φ.

III. Source Current Control Strategy

A. d-Axis Control

The above analysis shows that the steady-state value of the source current's d-axis component is determined by loads and cannot be controlled directly. But its harmonic component can be inhibited by suppressing $\Delta i_{\rm fd}$. Due to the ac nature of harmonics in d-axis, a PR controller is a good choice for the system to realize closed-loop control. For the IMC-based VSCF generation system, the frequencies of source current's harmonics in dq coordinates are high and time varying, which call for the PR controller used in the system being able to set different phase compensation angles at different frequencies, adapt itself to the time-varying frequency, and reduce the influence of the frequency detection error. To meet these requirements, the STRC with a phase compensator and a damping coefficient is adopted, whose expression is displayed in (17), which is same as that of the PR controller

$$G_{\rm STRC}(s) = \frac{K_r \zeta_k (k_h \omega_{\rm in})[s\cos\varphi_k - (k_h\omega_{\rm in})\sin\varphi_k]}{s^2 + 2\zeta_k(k_h\omega_{\rm in})s + (k_h\omega_{\rm in})^2} \quad (17)$$

where K_r is the coefficient of the STRC, which is used for adjusting the amplitude of the controller output; ζ_k is the damping coefficient for antiinterference; $k_h\omega_{\rm in}$ is the resonant frequency, which varies with input frequency; k_h represents the harmonic order; the cutoff frequency ω_c is equal to $k_h\zeta_k\omega_{\rm in}$; and φ_k is the compensation angle, which is equal to $k_\varphi \omega_{\rm in} T_s$, namely, k_φ times of digital control delay.

Different from traditional resonant controller, the STRC has two input variables rather than one, namely, the error and the time-varying resonant frequency. The function of the controller is realized by two integrators. The coefficients of the integrators and resonant frequency change simultaneously, so as to make a timely response to the time-varying ac signal. When resonant frequency changes at a not very fast speed, the STRC is equivalent to the combination of a group of PRs with different resonant frequencies. Its bode diagram is depicted in Fig. 5 when $K_r = 100$, $\varphi_k = 0$, $k_h\zeta_k\omega_{\rm in} = 2$, and $k_h\omega_{\rm in}$ changes from $750\times 2\pi$ to $1050\times 2\pi$. It can be noticed that the large gain is always produced at resonant frequency regardless of its variation, which ensures zero steady-state error at these frequencies.

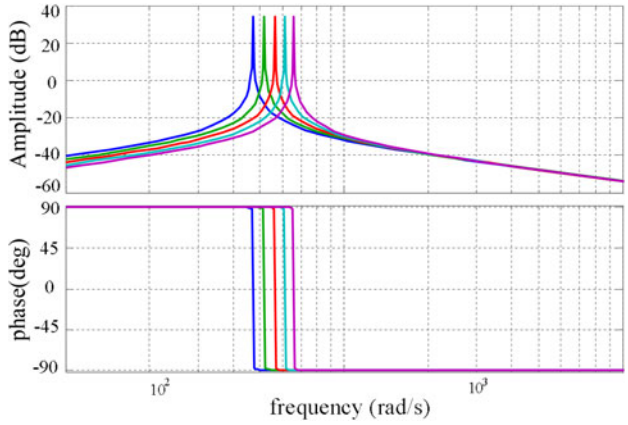

Fig. 5. Bode diagram of an STRC.

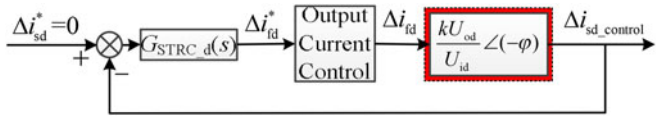

Fig. 6. Closed-loop control diagram of source current's d-axis harmonics.

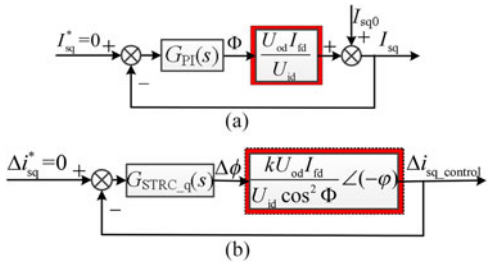

Fig. 7. Closed-loop control diagram of q-axis harmonics. (a) Closed-loop control diagram of the steady-state component. (b) Closed-loop control diagram of harmonics.

A combination of only five PRs with different resonant frequencies is depicted, for example, to show the function of the STRC. But, in fact, the STRC can track the ac signal all the time in the process of frequency variation.

After executing the closed-loop current control in IMC's output side, output current $\Delta i_{\rm fd}$ follows its reference value $\Delta i_{\rm fd}^*$. In accordance with the relationship between the source current and the output current shown in (14), the closed-loop control diagram of source current's d-axis harmonics is depicted in Fig. 6, where phasor $\frac{kU_{\rm od}}{U_{\rm id}}\angle(-\varphi)$ is the equivalent transfer function from $\Delta i_{\rm fd}$ to $\Delta i_{sd\_{\rm control}}$. The STRC is used for inhibiting the harmonics. With the phase compensator, the STRC can compensate the phase angle difference φ between source and output current's harmonics.

B. q-Axis Control

Expression (16) shows that the q-axis dc component of source current can be controlled through Φ in the condition of input/output voltage and load keeping constant, namely, system input power factor control [25]. The dc value can use a PI controller to track the reference, and the equivalent control block diagram is shown in Fig. 7(a). In order to ensure the security

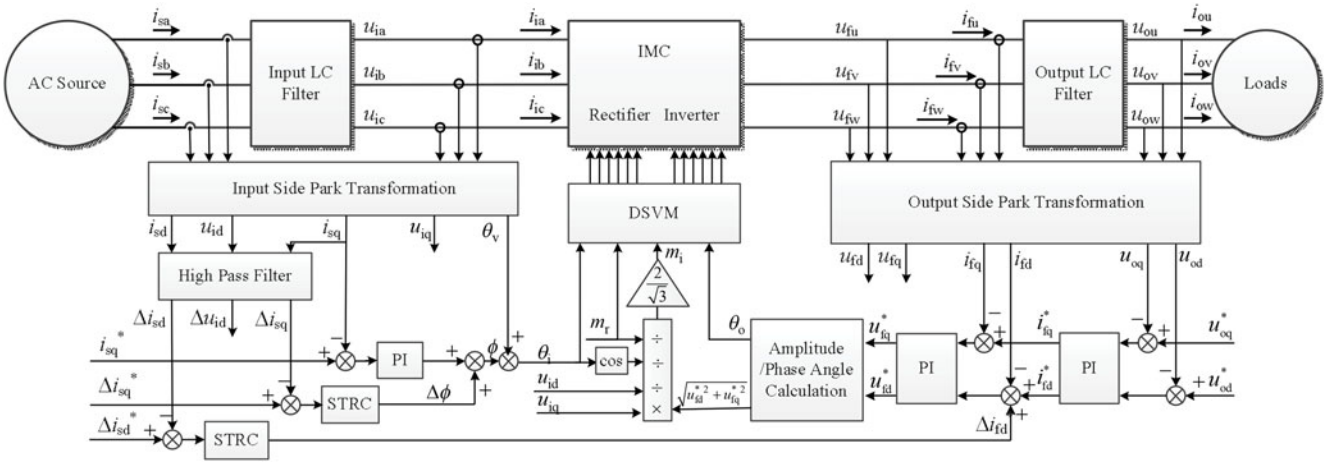

Fig. 8. Closed-loop control diagram of the IMC-based VSCF generation system.

of the system, the correctable displacement angle Φ should be within the scope of [-π/6, π/6] when DSVM is applied to the IMC [26].

It can be learnt from (15) that the controllable part of q-axis harmonic of source current is only related to $\Delta\dot{\Phi}$. $\Delta i_{sq\_\mathrm{control}}$, same as $\Delta i_{sd\_\mathrm{control}}$, is an ac value in dq coordinates and can be controlled by the STRC. The equivalent control diagram is shown in Fig. 7(b). The parts circled by red boxes in Fig. 7 are the equivalent transfer functions determined by the IMC.

Fig. 8 shows the closed-loop control diagram of the IMC-based VSCF generation system, where θ_v, θ_i, and θ_o are the phase angles of input voltage, input current, and output voltage synthetic vector, respectively. The diagram can be divided into three parts, that is, the left part of the source current control, the middle part of DSVM, and the right part of output voltage/current control, among which the source current control is the focus of this paper. In the left part, high-pass filters are needed for source current's d-/q-axis to obtain the feedbacks of the harmonics because their dc components are positive. Digital second-order high-pass filters are used in this paper, whose cutoff frequencies are equal to 45.5 Hz, which is determined by filtering effects. The control results of q-axis are used to correct the included angle between input voltage and current from unity to inductive to compensate for the capacitive input filter, and the control result of d-axis needs to be fed forward to the reference of output current, obtaining the modulation signals through the output current controller. Therefore, the closed-loop control of the output side is added into the control diagram. The results of the input/output controller are converted into duty ratios through the middle part of DSVM.

IV. System Stability Analysis

The input side of the IMC is connected with an *LC* filter for the purpose of reducing source current ripple caused by switching. The second-order system is prone to oscillation due to the small parasitic impedance of the line. In order to guarantee the system stability, the inductor is connected in parallel with a damping resistor, as shown in Fig. 2. However, the source current

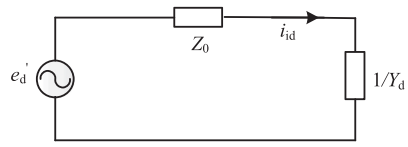

Fig. 9. Equivalent circuit of the input side.

control strategy proposed above for low-order harmonics trigged by asymmetric modulation will change the input impedance of the IMC to a certain extent, which may cause input filter resonance, increase high-order harmonics, and even make an effect on system stability. Thus, the impacts of the proposed control strategy on the resonance of the input filter and the system stability are analyzed in the following.

A. System Stability Analysis Without Source Current Control

The IMC is approximated as an impedance for investigating the influence of the source current control on the system stability. IMC input admittances in *dq* coordinates can be derived from (4):

$$Y_d = \frac{\Delta i_{\mathrm{id}}(s)}{\Delta u_{\mathrm{id}}(s)} = -\frac{U_{\mathrm{fd}} I_{\mathrm{fd}}}{U_{\mathrm{id}}^2} \tag{18}$$

$$Y_q = \frac{\Delta i_{\mathrm{iq}}(s)}{\Delta u_{\mathrm{iq}}(s)} = \frac{U_{\mathrm{fd}} I_{\mathrm{fd}}(1+\sec^2\Phi)}{U_{\mathrm{id}}^2} \tag{19}$$

where sec is short for secant, the reciprocal of cosine.

When the IMC-based VSCF generation system works in motor mode, I_{fd} has the same sign with U_{fd}, $Y_d < 0$, $Y_q > 0$. In this case, instability is easy to occur in d-axis. Thus, the d-axis is taken as an example to analyze the stability. The q-axis stability is checked later.

By regarding IMC as an impendence, the Thevenin equivalent circuit of the input side is displayed in Fig. 9 [27], where e_d' is the equivalent source voltage, and Z_0 is the equivalent impendence of the filter. Their expressions are shown as follows:

$$e_d'(s) = \frac{L_s s + R_d + R_s}{L_s R_d C_s s^2 + (R_s R_d C_s + L_s)s + (R_s + R_d)} e_d \tag{20}$$

$$Z_0(s) = \frac{R_d L_s s + R_d R_s}{L_s R_d C_s s^2 + (R_s R_d C_s + L_s)s + (R_s + R_d)}. \tag{21}$$

The expression of IMC's source current can be derived from Fig. 9 and (11):

$$i_{\mathrm{sd}}(s) = \frac{e'_d(s)}{Z_0(s) + 1/Y_d} G_{\mathrm{LC}}(s). \tag{22}$$

After substituting (11), (18), (20), and (21) into (22), the pole map of (22) with different damping resistance R_d is pictured in Fig. 10(a). It shows that with the decreasing of the damping resistance, namely, the increasing of the damping effect, the poles of $i_{\mathrm{sd}}(s)$ shift from positive half plane to negative half plane, and the system becomes stable. Fig. 10(a) verifies the necessity of adding a damping resistor to the input filter and is helpful to determine the actual damping resistance.

B. Influence of d-Axis STRC's Parameters on the Stability

When d-axis current control is added, its STRC's output can be expressed as

$$g(u_{\mathrm{id}}(s)) = G_{\mathrm{STRC\_d}}(s) \frac{\tau s}{\tau s + 1} \frac{1}{L_s s + R_s} (u_{\mathrm{id}}(s) - e_d(s)) \tag{23}$$

where τ is the coefficient of the digital filter. Feeding (23) forward to the output current reference, the output current i_{fd} in (4) can be modified to $i_{\mathrm{fd}}^{**} = i_{\mathrm{fd}} + g(u_{\mathrm{id}})$. The input d-axis admittance is modified as follows:

$$Y'_d = \frac{U_{\mathrm{fd}} U_{\mathrm{id}} \partial g - U_{\mathrm{fd}} I_{\mathrm{fd}}}{U_{\mathrm{id}}^2} \tag{24}$$

where $\partial g = G_{\mathrm{STRC\_d}}(s) \frac{\tau s}{\tau s+1} \frac{1}{L_s s + R_s}$.

Replace Y_d in (22) with (24), in which $e'_d(s)$, $Z_0(s)$, and $G_{\mathrm{LC}}(s)$ are determined when input filter parameters are decided; the coefficient of the digital filter, τ, depends on the filtering effect. As a result, d-axis STRC's parameters are the only influential factors of pole distribution of $i_{\mathrm{sd}}(s)$, namely, system stability.

STRC's compensation angle φ_k, which is equal to k_φ times of the digital control delay, is used to compensate for the digital control delay and the phase lag caused by the input filter. The phase lag caused by the digital control delay is one time of $\omega_{\mathrm{in}} T_s$ all the time; the phase lag caused by the input filter will change along with frequency, which can be learnt from the phase frequency curve (line 1) in Fig. 4. According to the curve, the specific phase lag angle at a given frequency can be obtained. Then, the value of $(k_\phi - 1)$ can be calculated by dividing the angle with $\omega_{\mathrm{in}} T_s$. Another phase frequency curve of lagging $\omega_{\mathrm{in}} T_s$ behind is drawn in line 2 in Fig. 4. It can be found that after comparing the two curves, that phase lag caused by the filter is less than $\omega_{\mathrm{in}} T_s$ when harmonic frequency is smaller than input filter's resonant frequency. In conclusion, $1 < k_\varphi < 2$. When the input frequency $f_{\mathrm{in}} = 300$ Hz, the phase compensation angle is equal to $\omega_{\mathrm{in}} T_s$ for 900-Hz $(3\omega_{\mathrm{in}})$ harmonic because $3\omega_{\mathrm{in}} < \omega_1$; and the phase compensation angle is equal to $1.46\omega_{\mathrm{in}} T_s$ for 1800-Hz $(6\omega_{\mathrm{in}})$ harmonic.

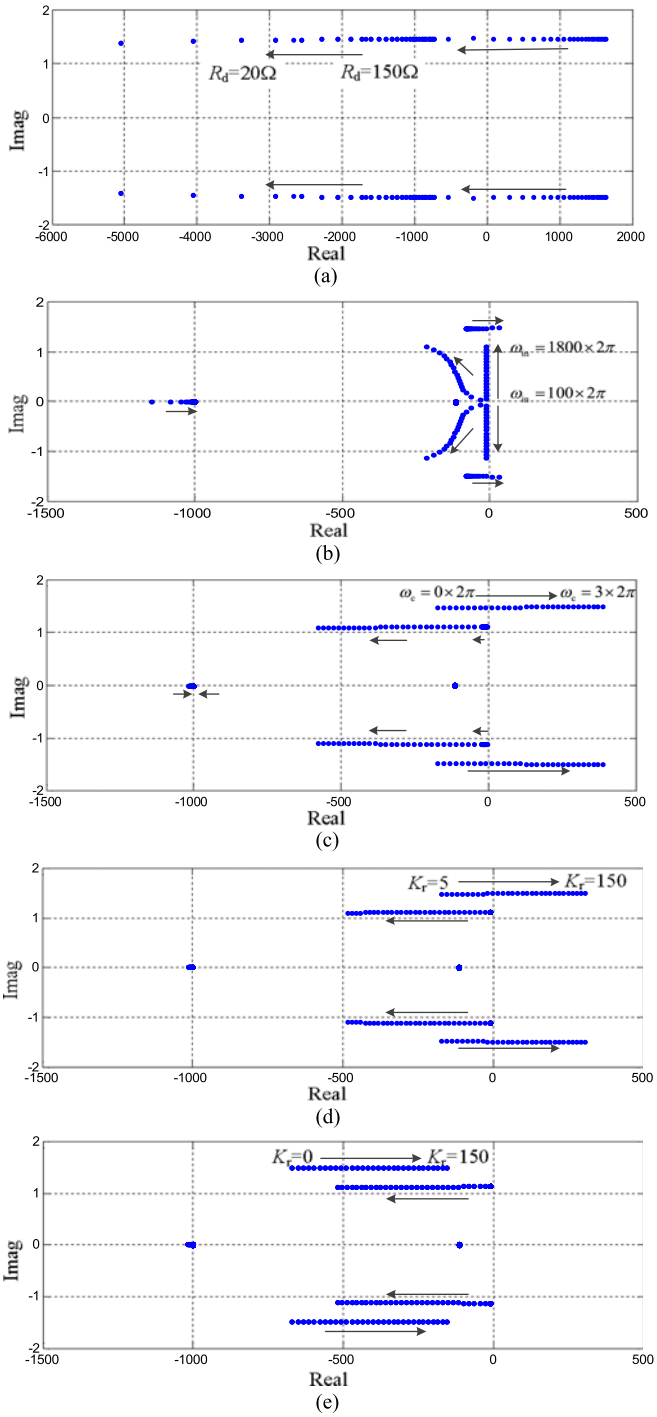

Fig. 10. System pole maps with different parameters of the d-axis resonant controller. (a) Different damping resistance R_d. (b) Different resonant frequency $k_h \omega_{\mathrm{in}}$. (c) Different cutoff frequency ω_c. (d) Different coefficient of resonant K_r. (e) Different coefficient of resonant K_r after adding active damping.

Fig. 10(b) plots the pole map of $i_{\mathrm{sd}}(s)$ under the condition that K_r, ω_c, and φ_k are constant and the resonant frequency $k_h \omega_{\mathrm{in}}$ changes from $100 \times 2\pi$ to $1800 \times 2\pi$. The arrow points at the poles' moving direction when resonant frequency increases. It can be learnt from the figure that the stability of the system is deteriorated with the increase of $k_h \omega_{\mathrm{in}}$. However, the resonant frequency is determined by the frequency of current harmonics, that is, $3\omega_{\mathrm{in}}$ and $6\omega_{\mathrm{in}}$, respectively, in this paper. As a result, the

stability of the system adding STRC with a resonant frequency of $6\omega_{\rm in}$ needs to be checked first. Then, the system will be stable after adding STRC with low resonant frequency.

Fig. 10(c) shows the pole map of $i_{\rm sd}(s)$ with the cutoff frequency ω_c changing on the condition that φ_k, K_r, and $k_h\omega_{\rm in}$ keep constant. It can be seen that the stability of the system gets worse with the increase of cutoff frequency. Therefore, the selection of the cutoff frequency ω_c needs to balance the system stability and the antiinterference ability.

Fig. 10(d) displays the pole map of $i_{\rm sd}(s)$ with a coefficient of resonant K_r varying under the condition that φ_k, $k_h\omega_{\rm in}$, and ω_c are constant. When K_r increases from 5 to 150 little by little, two poles of $i_{\rm sd}(s)$ move gradually to the right half plane, which signifies worse stability. Nevertheless, K_r determines the output amplitude of the STRC. If K_r is too small, the amplitude of STRC's output is low, resulting in undesirable effect on harmonic suppression; if K_r is too large, the system will be unstable. In order to realize effective harmonic inhibition, maintain system stability, and keep the ability of inhibiting harmonics of switching frequency, this paper adopts the active damping algorithm proposed in [21] to feed $\Delta u_{\rm id}$ forward to $i_{\rm fd}$ to strengthen the system stability. After adding active damping control, input *d*-axis admittance of the IMC can be modified as

$$Y_d'' = \frac{U_{\rm fd}U_{\rm id}(\partial g + k_d\frac{\tau s}{\tau s+1}) - U_{\rm fd}I_{\rm fd}}{U_{\rm id}^2} \tag{25}$$

where k_d is the active damping coefficient. When $k_d = 0.02$ and other parameters remain the same with Fig. 10(d), the pole map of $i_{\rm sd}(s)$ with K_r changing is shown in Fig. 10(e). The contrast between Fig. 10(d) and (e) shows that after adding active damping, K_r can be a greater value, providing the possibility to suppress larger harmonics in the *d*-axis.

C. Influence of q-Axis STRC's Parameters on the Stability

Current control result of the q-axis is used for correcting the phase angle of input current synthetic vector, where the PI controller outputs a constant dc value Φ to correct the input power factor, whose value has nothing to do with $u_{\rm iq}$; the STRC outputs an ac value to suppress the current ripple, which is the function of $u_{\rm iq}$. The displacement angle in (4) can be expressed as $\phi^{**} = \Phi + f(u_{\rm iq})$. The *q*-axis admittance after adding current control can be expressed as

$$Y_q' = \frac{U_{\rm fd}I_{\rm fd}}{U_{\rm id}^3\cos^2\delta}(U_{\rm id}\cos^2\delta + U_{\rm id} + \partial f) \tag{26}$$

where $\partial f = G_{\rm STRC\_q}(s)\frac{\tau s}{\tau s+1}\frac{1}{L_s s+R_s}$.

Substituting (26) into the *q*-axis current equation, which is the same as (22), the pole maps of $i_{\rm sq}(s)$ are displayed in Fig. 11, where $k_h\omega_{\rm in}$, K_r, and Φ change, respectively, in (a)–(c). In Fig. 11, the real parts of the poles near $j\omega$-axis are about –6.2, which change inconspicuously along with $k_h\omega_{\rm in}$, K_r, and Φ, are always less than 0. Therefore, the system will always be stable after adding *q*-axis current control.

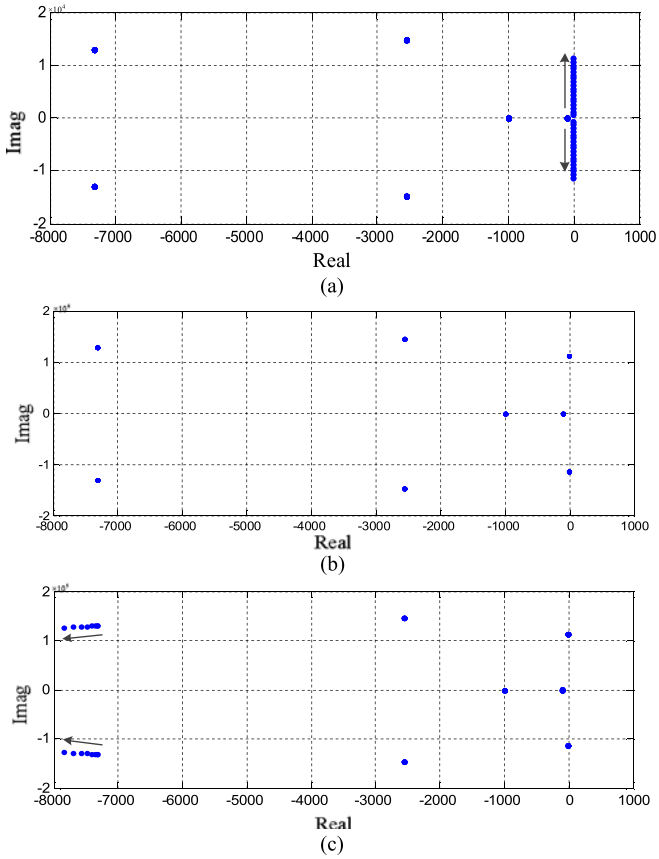

Fig. 11. System pole maps with different parameters of the *q*-axis resonant controller. (a) Different resonant frequency $k_h\omega_{\rm in}$. (b) Different coefficient of resonant K_r. (c) Different input power factor.

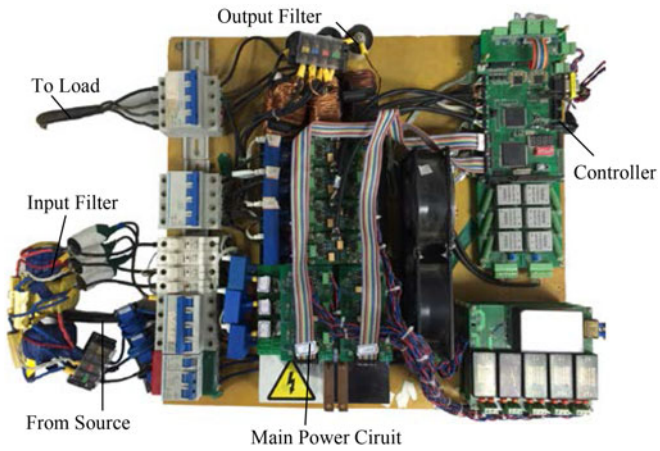

Fig. 12. Prototype of the IMC-based VSCF generation system.

V. Experimental Results

A prototype of the IMC-based VSCF generation system, as shown in Fig. 12, has been built to verify the effectiveness of the proposed source current control strategy. The rectifier stage of the prototype is composed of two insulated-gate bipolar transistor (IGBT) modules (APTGF50TDU120PG, Microsemi), and the inverter stage is composed of six discrete IGBT devices (FGA25N120ANTD, Fairchild). Photocouplers

TABLE I
PARAMETERS OF THE IMC-BASED VSCF GENERATION SYSTEM

Parameters	Symbols	Units	Values
Effective value of the source voltage	e_a, e_b, e_b	V	115
Input frequency range	$f_{\rm in}$	Hz	250–350
The input filter inductance	$L_{\rm s}$	mH	0.9
Parallelled damping resistance of the input filter inductor	$R_{\rm d}$	Ω	40
The input filter capacitance	$C_{\rm s}$	μF	5
Output frequency	f_o	Hz	100
The output filter inductance	L_f	mH	1.2
The output filter capacitance	$C_{\rm f}$	μF	10.0
Switching frequency	f_s	kHz	20
Load resistance	R_L	Ω	10
Load inductance	L_L	mH	0.56

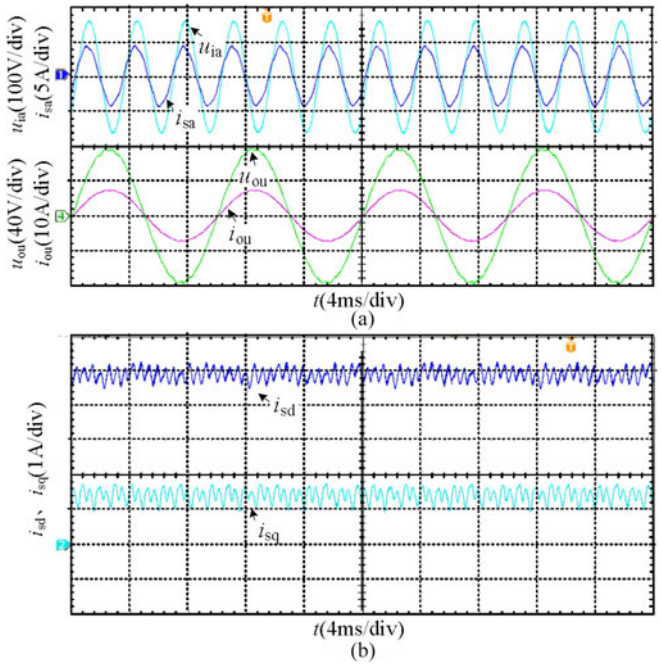

Fig. 13. Experimental waveforms of (a) $u_{\rm ia}$, $i_{\rm sa}$, $u_{\rm ou}$, and $i_{\rm ou}$ and (b) $i_{\rm sd}$ and $i_{\rm sq}$, without source current control.

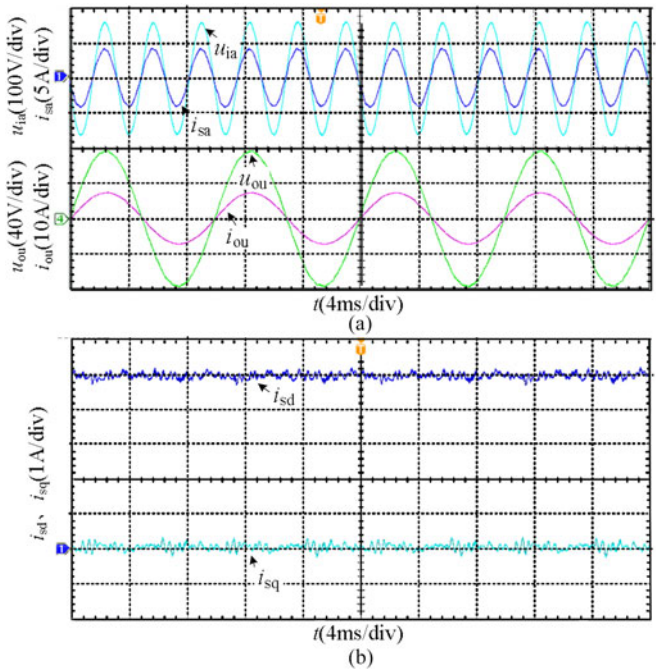

Fig. 14. Experimental waveforms of (a) $u_{\rm ia}$, $i_{\rm sa}$, $u_{\rm ou}$, and $i_{\rm ou}$ and (b) $i_{\rm sd}$ and $i_{\rm sq}$, with source current control.

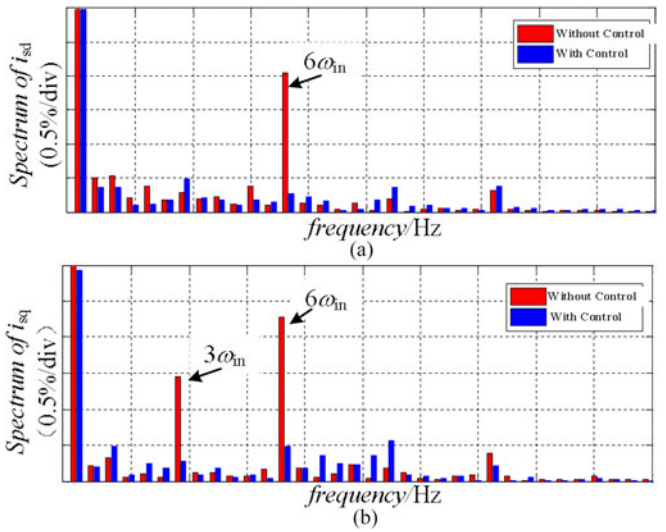

Fig. 15. Spectra of experimental waveforms with and without source current control of (a) $i_{\rm sd}$ and (b) $i_{\rm sq}$.

(TLP250, TOSHIBA), with transistor totem-pole circuits on the output, are used to drive these IGBTs. The total delay of the drive signals is about a few hundreds of nanoseconds and is roughly compensated by the controller. The proposed algorithm is implemented using DSP (TMS320F28335, TI) and CPLD (XPLD5512MV, Lattice) devices. A programmable three-phase ac power source (61511, Chroma) is utilized to provide ac voltages for simplicity. The parameters used in the experiment are described in Table I.

Experiments are carried out to verify the source current control at a fixed input frequency first. The input frequency is set to 300 Hz, and the output voltage is set to 57.5 V. Fig. 13(a) shows the experimental waveforms of the IMC's input voltage $u_{\rm ia}$, source current $i_{\rm sa}$, load voltage $u_{\rm ou}$, and load current $i_{\rm ou}$ without source current control. Fig. 13(b) shows the waveforms of $i_{\rm sd}$ and $i_{\rm sq}$ without source current control. It can be seen from the figures that $i_{\rm sa}$ leads $u_{\rm ia}$ a certain phase and $i_{\rm sq}$ has an obvious dc component, which means that the capacitive reactive current is contained in the source current and the input power factor is not equal to 1. $i_{\rm sa}$ distorts with sharp wave heads, and its *dq* components $i_{\rm sd}$ and $i_{\rm sq}$ oscillate severely. The red bars in Fig. 15 demonstrate the spectra of $i_{\rm sd}$ and $i_{\rm sq}$. As can be seen, the spectra are identical to aforementioned conclusions: the spectrum peak of $i_{\rm sd}$ appears at the frequency of $6\omega_{\rm in}$; the harmonics of $i_{\rm sq}$ are mainly third and sixth order.

Three STRCs, which take the system stability and the harmonic suppression effect into consideration, are designed to

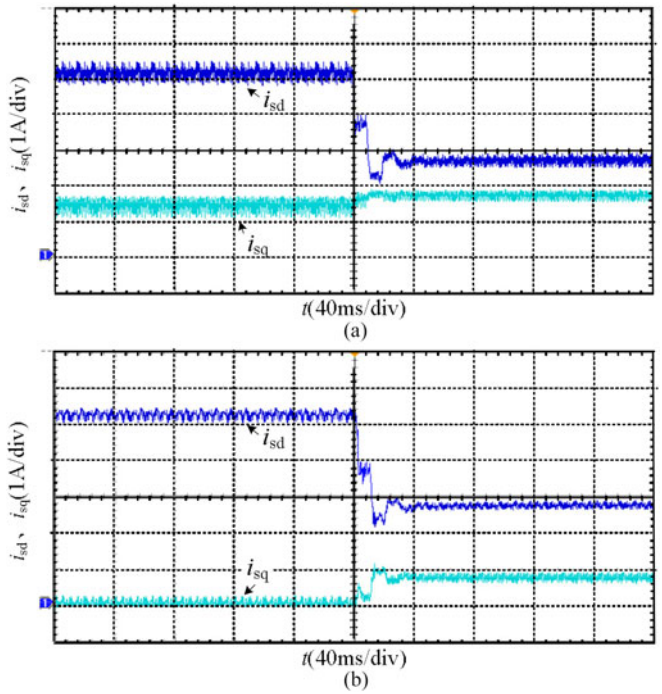

Fig. 16. Experimental waveforms of i_{sd} and i_{sq} when load decreases: (a) without source current control and (b) with source current control.

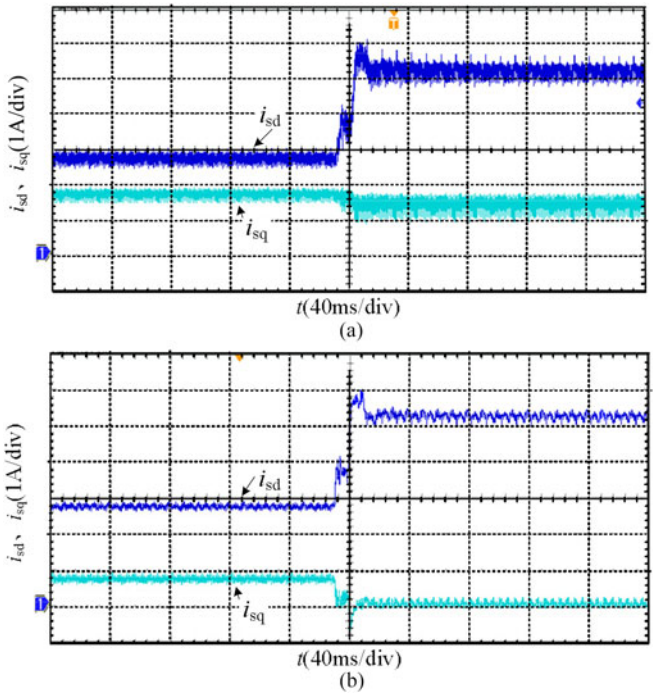

Fig. 17. Experimental waveforms of i_{sd} and i_{sq} when load increases: (a) without source current control and (b) with source current control.

eliminate these harmonics, whose parameters are listed as follows:

d-axis: $k_\phi = 1.46$; $k_h\omega_{\mathrm{in}} = 1800$ Hz; $\omega_c = 2$ rad/s; $K_r = 150$; $k_d = 0.02$;

q-axis_1: $k_\phi = 1$; $k_h\omega_{\mathrm{in}} = 900$ Hz; $\omega_c = 2\mathrm{rad/s}$; $K_r = 15$;

q-axis_2: $k_\phi = 1.46$; $k_h\omega_{\mathrm{in}} = 1800$ Hz; $\omega_c = 2$ rad/s; $K_r = 50$.

After implementing the source current control in the same condition, corresponding current and voltage waveforms are displayed in Fig. 14. Comparing waveforms of Fig. 14 with those of Fig. 13, it is obvious that the dc component of i_{sq} decreases to 0, with i_{sa} keeping the same phase with u_{ia}, which means that the input power factor has been corrected to 1. The oscillations of i_{sd} and i_{sq} are diminished, only remaining minor high-frequency vibration. The spectra of i_{sd} and i_{sq} are shown in Fig. 15 in blue bars, implying that the sixth-order harmonic in i_{sd} and third and sixth-order harmonics in i_{sq} decrease. The distortion of i_{sa} is suppressed effectively when the source current control is adopted, with its total harmonic distortion (THD) decreasing from 5.2% to 2.5%. At the same time, the output voltage waveform is slightly improved, with its THD decreasing from 1.34% to 0.99%.

Considering that the system's loads will change on some occasions, experimental tests with a 50% decrease of the load current amplitude without and with source current control are carried out. The waveforms are shown in Fig. 16. It can be seen from Fig. 16(a) that when the load current amplitude decreases, harmonics amplitudes in source current *d*-/*q*-axis components decrease simultaneously to a certain extent, which are in accordance with the above analysis shown in (14) and (15). After adopting the proposed source current control strategy, the system can still remain stable, and harmonics in both i_{sd} and i_{sq} are suppressed with their amplitudes decreasing whatever operates in full loads or in half loads or even in the process of transition. However, influenced by the reducing active power, the input power factor angle exceeds the range of [-π/6, π/6] before the source current control is added. In order to ensure the safety of the system, only the maximum angle, π/6, is corrected in the input side, and the corrected input power factor is less than 1. The dc component of i_{sq} in Fig. 16(b) is lower than that in Fig. 16(a), but does not equal to zero. Experiments with load changing from half to full are also carried out, whose waveforms are shown in Fig. 17. Corresponding verdicts as Fig. 16 can be concluded by comparing Fig. 17(a) with (b).

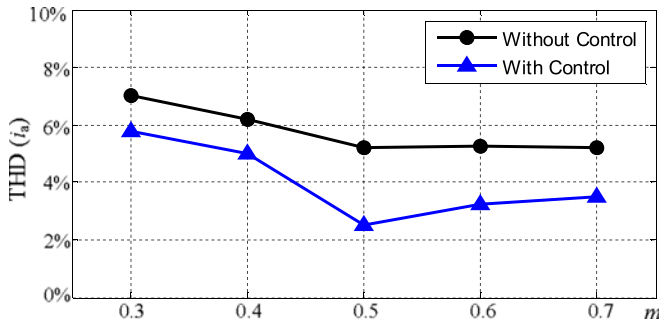

Fig. 18. THD values of i_{sa} without and with source current control.

Above experimental tests are all carried out in the condition of modulation ratio *m* being 0.5. To verify the applicability of the proposed strategy, contrast experiments with different modulation ratios are also carried out in this paper. Their source currents' THD values and input power factors are calculated. Fig. 18 shows i_{sa}'s THD curves versus *m*. It can be seen from the figure that THDs of i_{sa} are reduced in all conditions after employing the proposed control strategy. Input power factor

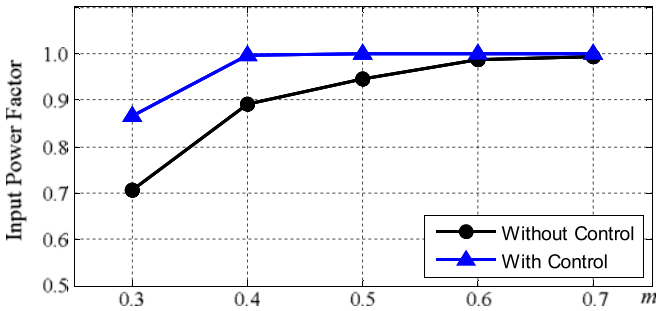

Fig. 19. Input power factor without and with source current control.

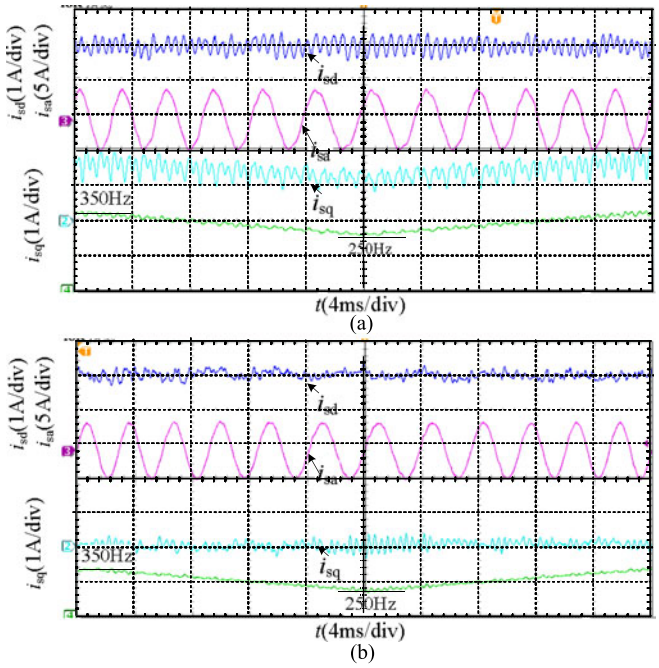

Fig. 20. Experimental waveforms of $i_{\rm sd}$, $i_{\rm sa}$, and $i_{\rm sq}$: (a) without source current control and (b) with source current control.

curves versus m are displayed in Fig. 19. IMC's output voltage and current will rise with the increase of the modulation index, leading to a larger $i_{\rm sd}$ due to the principle of power balance. As a result, the input power factor will increase along with m without control, as shown by the black curve. Comparing the two curves in Fig. 20, it can be concluded that input power factors are increased via source current control. In most cases, system's input power factor can be corrected to 1, but if the input power factor angle is larger than $\pi/6$ without control, such as $m = 0.3$, after employing the proposed control, its power factor increases but is not equal to 1.

Apart from fixing the input frequency, the source current control proposed in this paper is also suitable for variable-input-frequency condition. Fig. 20 shows the experimental waveforms of the source current $i_{\rm sa}$ and its dq components $i_{\rm sd}$ and $i_{\rm sq}$ when input current frequency changes between 250 and 350 Hz, without and with source current control, respectively, in which channel 4 indicates the input frequency. Generated mainly by the input filter capacitor, the capacitive reactive current will vary with input frequency without control, in accordance with the waveform of $i_{\rm sq}$ in Fig. 20(a). Meanwhile, $i_{\rm sd}$ and $i_{\rm sq}$ contain large harmonic components with $i_{\rm sa}$ distorted. The experimental waveforms of $i_{\rm sa}$, $i_{\rm sd}$, and $i_{\rm sq}$ are displayed in Fig. 20(b) after employing the source current control. In contrast to Fig. 20(a), the dc component of $i_{\rm sq}$ is reduced to 0 at any time, indicating that the input power factor has been corrected to 1. Moreover, harmonics in $i_{\rm sd}$ and $i_{\rm sq}$ are suppressed in terms of the reduction of their peak–peak amplitudes. And the quality of $i_{\rm sa}$ is also improved. The validity and the feasibility of the source current control are thus verified.

VI. Conclusion

This paper has studied the source current control strategy as well as its influence on the system stability of the VSCF generation system, which has high-source-frequency and wide-frequency-variation range. The following points summarize the work presented in this paper.

1) Source current harmonics in dq coordinates are analyzed, including frequency analysis and expressions analysis. The results indicate that when the IMC is connected to constant power loads, the only uncontrollable part of the source current is its d-axis dc component. Its q-axis dc component and their harmonics are controllable.
2) A source current control strategy is proposed in this paper for an IMC with asymmetric modulation and high source frequency. It can suppress low-order harmonics, improve waveforms' quality, and correct the input power factor. The experimental results verify the validity and the feasibility of the proposed strategy.
3) The impact of the proposed control strategy on the resonance of the input filter and the system stability is discussed, drawing a conclusion that the d-axis control will deteriorate the stability of the system, while the q-axis will not when the power flows from source to loads. The system stability and the harmonic suppression effect should be taken into consideration for selecting the parameters of the STRC. With proper control parameters, harmonics produced by modulation are suppressed, while harmonics trigged by input resonance have no significant changes.

References

[1] S. F. Pinto, P. Alcaria, J. Monteiro, and J. Fernando Silva, "Matrix converter-based active distribution transformer," *IEEE Trans. Power Del.*, vol. 31, no. 4, pp. 1493–1501, Aug. 2016.
[2] J. Lei *et al.*, "Predictive power control of matrix converter with active damping function," *IEEE Trans. Ind. Electron.* vol. 63, no. 7, pp. 4550–4559, Jul. 2016.
[3] S. Liu, B. Ge, Y. Liu, H. Abu-Rub, R. S. Balog, and H. Sun, "Modeling, analysis, and parameters design of LC-filter-integrated quasi-Z-source indirect matrix converter," *IEEE Trans. Power Electron.*, vol. 31, no. 11, pp. 7544–7555, Apr. 2016.
[4] C. Garcia *et al.*, "A simple current control strategy for a four-leg indirect matrix converter," *IEEE Trans. Power Electron.*, vol. 30, no. 4, pp. 2275–2287, Apr. 2015.
[5] L. Empringham, W. Kolar, J. Rodriguez, P. W. Wheeler, and J. C. Clare, "Technological issues and industrial application of matrix converters: A review," *IEEE Trans. Ind. Electron.*, vol. 60, no. 10, pp. 4260–4271, Oct. 2013.
[6] A. Trentin, L. Empringham, L. De Lillo, P. Zanchetta, P. Wheeler, and J. Clare, "Experimental efficiency comparison between a direct matrix converter and an indirect matrix converter using both Si IGBTs and SiC MOSFETs," *IEEE Trans. Ind. Electron.*, vol. 52, no. 5, pp. 4135–4145, May 2016.

[7] S. Mondal and D. Kastha, "Improved direct torque and reactive power control of a matrix-converter-fed grid-connected doubly fed induction generator," *IEEE Trans. Ind. Electron.*, vol. 62, no. 12, pp. 7590–7598, Dec. 2015.

[8] J. Lei *et al.*, "Feedback control strategy to eliminate the input current harmonics of matrix converter under unbalanced input voltages," *IEEE Trans. Power Electron.* vol. 32, no. 1, pp. 878–888, Jan. 2017.

[9] J. Kolar, T. Friedli, J. Rodriguez, and P. W. Wheeler, "Review of three phase PWM ac-ac converter topologies," *IEEE Trans. Ind. Electron.*, vol. 58, no. 11, pp. 4988–5006, Nov. 2011.

[10] J. Haruna and J. Itoh, "Behavior of a matrix converter with a feedback control in an input side," in *Proc. Int. Power Electron. Conf.*, Sapporo, Japan, 2010, pp. 1202–1207.

[11] M. Rivera *et al.*, "Review of predictive control methods to improve the input current of an indirect matrix converter," *IET Power Electron.* vol. 7, no. 4, pp. 886–894, 2014.

[12] X. Qin, B. Zhou, J. Wei, and J. Lei, "Distortion analysis and duty ratio correction algorithm for asymmetric modulation of two-stage matrix converter," *IEEE Trans. Ind. Electron.*, vol. 62, no. 1, pp. 351–362, Mar. 2015.

[13] C. Tarasantisuk, T. Suyata, V. Tarateeraseth, and K. Witheephanich, "Active and reactive power control for three-phase grid inverters with proportional resonant control strategies," in *Proc. 13th Int. Conf. Elect. Eng./Electron., Comput., Telecommun. Inf. Technol.*, Chiang Mai, Thailand, 2016, pp. 1–6.

[14] D. Dong, D. Xu, and M. Xu, "Experiment comparison of repetitive control and resonant control," in *Proc. IEEE 8th Int. Power Electron. Motion Control Conf.*, Hefei, China, May 22–25, 2016, pp. 2150–2155.

[15] Y. Yang, K. Zhou, M. Cheng, and B. Zhang, "Phase compensation multi resonant control of CVCF PWM converters," *IEEE Trans. Power Electron.*, vol. 28, no. 8, pp. 3923–3930, Aug. 2013.

[16] Y. Yang, K. Zhou, and M. Cheng, "Phase compensation resonant controller for PWM converters," *IEEE Trans. Ind. Electron.*, vol. 9, no. 2, pp. 957–964, May 2013.

[17] Q. Qian, J. Xu, S. Xie, and L. Ji, "Analysis and improvement of harmonic quasi resonant control for LCL-filtered grid-connected inverters in weak grid," in *Proc. IEEE Appl. Power Electron. Conf. Expo.*, Mar. 20–24, 2016, pp. 3446–3452.

[18] Z. Su, D. Wang, J. Chen, X. Zhang, and L. Wu, "Improving operation performance of magnetically suspended flywheel with PM-biased magnetic bearing using adaptive resonant controller and nonlinear compensation method," *IEEE Trans. Magn.*, vol. 52, no. 7, Jan. 2016, Art. no. 8300304.

[19] R. Cardenas, E. Espina, J. Clare, and P. Wheeler, "Self-tuning resonant control of a seven-leg back-to-back converter for interfacing variable-speed generators to four-wire loads," *IEEE Trans. Ind. Electron.*, vol. 62, no. 7, pp. 4618–4629, Jul. 2015.

[20] J. Lei, B. Zhou, X. Qin, J. Wei, and J. Bian, "Active damping control strategy of matrix converter via modifying input reference currents," *IEEE Trans. Power Electron.* vol. 30, no. 9, pp. 5260–5271, Sep. 2015.

[21] M. Rivera, J. Rodriguez, and B. Wu, "Current control for an indirect matrix converter with filter resonance mitigation," *IEEE Trans. Ind. Electron.*, vol. 59, no. 1, pp. 71–79, Jan. 2012.

[22] L. Helle, K. B. Larsen, A. H. Jorgensenm, S. Munk-Nielsen, and F. Blaabjerg, "Evaluation of modulation schemes for three-phase to three-phase matrix converters," *IEEE Trans. Ind. Electron.*, vol. 51, no. 1, pp. 158–171, Feb. 2004.

[23] H. Hidenori and Y. Eiji, "Improvement of output voltage control performance for low-speed operation of matrix converter," *IEEE Trans. Power Electron.*, vol. 20, no. 6, pp. 1372–1378, Nov. 2005.

[24] X. Qin, B. Zhou, J. Lei, and N. Han, "Input filter design for two-stage matrix converter applied in aero variable-frequency power system," in *Proc. IEEE 40th Annu. Conf. Ind. Electron.*, Dallas, TX, USA, Oct. 29–Nov. 1, 2014, pp. 4852–4858.

[25] H. M. Nguyen, H.-H. Lee, and T.-W. Chun, "Input power factor compensation algorithms using a new direct-SVM method for matrix converter," *IEEE Trans. Ind. Electron.*, vol. 58, no. 1, pp. 232–243, Jan. 2011.

[26] F. Scafmeister and J. W. Kolar, "Novel hybrid modulation schemes significantly extending the reactive power control range of all matrix converter topologies with low computational effort," *IEEE Trans. Ind. Electron.*, vol. 59, no. 1, pp. 194–210, Jan. 2012.

[27] Y. Sun, M. Su, X. Li, H. Wang, and W. Gui, "A general constructive approach to matrix converter stabilization," *IEEE Trans. Power Electron.*, vol. 28, no. 1, pp. 418–431, Jan. 2013.

Na Han was born in Zhejiang, China, in 1991. She received the B.S. degree in electrical engineering in 2014 from Nanjing University of Aeronautics and Astronautics, Nanjing, China, where she has been working toward the M.S. degree since 2014.

Her main research interests include the design and control technology for matrix converters.

Bo Zhou was born in Wenzhou, Zhejiang Province, China, in 1961. He received the B.S. degree from Zhejiang University, Hangzhou, China, in 1983, the M.S. degree from Chongqing University, Chongqing, China, in 1986, both in automation, and the Ph.D. degree in power electriconics and power transmission from Nanjing University of Aeronautics and Astronautics (NUAA), Nanjing, China, in 2000.

He is a Professor with the College of Automation Engineering, NUAA, and is the Director of the Jiangsu Key Laboratory of New Energy Generation and Power Conversion. His research interests include power converter, electrical machine driving systems, and renewable power systems.

Prof. Zhou received of the State Technological Invention Second-Class Award in 2009, the Geneva International Invention Gold Award in 2011, and the Defense Technological Invention First Prize in 2008.

Jiang Yu was born in Zigui, China, in 1978. He received the B.S. degree in measurement and control technology and instruments from Xi'an University of Technology, Xi'an, China, and the M.S. degree in electrical engineering from Xi'an Jiaotong University, Xi'an, in 2001 and 2012, respectively.

He is a Senior Engineer at Shanxi Aero Electric Co., Ltd., Xingping, China, and a Lead Researcher in the Aviation key Laboratory of Science and Technology on Aerospace Power System, conducting research in power electronic technology and its application in aerospace power systems.

Xianhui Qin was born in Beijing, China, 1988. He received the B.S. degree in electrical engineering in 2009 and the Ph.D. degree in electrical engineering and electric drive in 2016 from Nanjing University of Aeronautics and Astronautics, Nanjing, China.

His main research interests include aeronautic static power conversion and the design and control technology for practical matrix converters.

Jiaxing Lei (S'14) was born in Sichuan, China, 1991. He received the B.S. degree in electrical engineering in 2012 from Nanjing University of Aeronautics and Astronautics, Nanjing, China, where he has been working toward the Ph.D. degree since 2012.

His main research interests include indirect matrix converters and its applications in aerospace power systems.

Yang Yang was born in Weinan, China, 1988. She received the B.S. and M.S. degrees in electrical engineering from Northwestern Polytechnical University, Xi'an, China, in 2011 and 2014, respectively.

She is an Engineer of electricity development at Shaanxi Aero Electric Co., Ltd., Xingping, China, and a member in the Aviation key Laboratory of Science and Technology on Aerospace Power System. Her research interests include simulation technology and its application in aerospace power systems.